



Impact of early spring sea ice in Barents Sea on midsummer rainfall distribution at Northeast China

Tingting Han^{1,2} · Minghua Zhang^{3,4} · Jiawen Zhu⁴ · Botao Zhou^{1,2} · Shangfeng Li⁵

Received: 10 September 2020 / Accepted: 29 March 2021 / Published online: 11 April 2021
© The Author(s), under exclusive licence to Springer-Verlag GmbH Germany, part of Springer Nature 2021

Abstract

The influence of early spring sea ice at Barents Sea on midsummer rainfall in Northeast China (NEC) is identified based on observational analyses and atmospheric modeling experiments in this study. Increased sea ice area (SIA) in the Barents Sea is ensued by positive rainfall anomalies at north of NEC and by negative anomalies at south, and vice versa. Specifically, due to a good seasonal persistence from spring to summer, the preceding sea ice anomalies exert an impact on midsummer surface air temperature anomalies and vertical stability over Barents Sea via the modulation on turbulent heat flux. The anomalous circulation is further triggered over Europe and the Mediterranean Sea through meridional vertical cells, with a barotropic structure. Accordingly, an effective Rossby wave source is excited over the eastern Mediterranean by the advection of vorticity by divergence wind, and causes an eastward propagation of Silk Road Pattern to East Asia. In addition, another SIA-related wave-like train can diffuse directly southeastward from Arctic to NEC in a polar path. Observations and numerical simulations indicate that, in response to increased sea ice at Barents Sea, an anomalous cyclone emerges over NEC, along with easterly or southeasterly over north of NEC and with northwesterly over south, leading to moisture convergence anomalies at north and divergence anomalies at south. Jointly, ascending (descending) motion anomalies favors a wet (dry) summer over north (south) of NEC.

Keywords Midsummer rainfall over Northeast China · Arctic sea ice · Rossby wave train · Predictor

1 Introduction

Northeast China (NEC), including Heilongjiang Province, Jilin Province, Liaoning Province and eastern four leagues of Inner Mongolia, is a major industrial base and breadbasket in China. Located at mid-to-high latitudes, NEC is one of the regions that are most vulnerable to global warming in China (Zhou et al. 2016). Climate change in this region, in terms of variability and spatial distribution of rainfall, has potential impacts on water resources, agricultural production, economic development and energy demand. Therefore, there is an urgent need to understand the rules governing the rainfall variation at NEC.

Summer rainfall at NEC is generally affected by atmospheric circulation regimes both at tropics and extratropics, such as East Asian monsoon systems (Han et al. 2015; Sun et al. 2017), sea surface temperature (SST) anomalies in the tropical Indian and Pacific oceans (Wang and He 2015; Han et al. 2017, 2018b), cold vortex activities (Hu et al. 2010; Shen et al. 2011), the Okhotsk High (Yao and Dong 2000) as well as the extension and intensity of Asian polar vortex

✉ Tingting Han
hantt08@126.com

- ¹ Collaborative Innovation Center On Forecast and Evaluation of Meteorological Disasters/Key Laboratory of Meteorological Disaster, Ministry of Education, Nanjing University for Information Science and Technology, Nanjing, China
- ² Institute of Atmospheric Physics, Nansen-Zhu International Research Centre, Chinese Academy of Sciences, Beijing, China
- ³ School of Marine and Atmospheric Sciences, Stony Brook University, Stony Brook, NY, USA
- ⁴ International Center for Climate and Environmental Sciences, Institute of Atmospheric Physics, Chinese Academy of Sciences, Beijing, China
- ⁵ Jilin Provincial Key Laboratory of Changbai Mountain Meteorology & Climate Change, Laboratory of Research for Middle-High Latitude Circulation Systems and East Asian Monsoon, Institute of Meteorological Sciences of Jilin Province, Changchun, China

(Wang and Ding 2009). In addition, the North Atlantic Oscillation exerts a strengthened impact on summer rainfall over NEC after the late 1970s (Sun and Wang 2012). Analysis of observation and numerical experiments has shown that the phase shift of the Pacific Decadal Oscillation (PDO) contributes to the recent decadal variation in summer rainfall at eastern and northeast China (Han et al. 2015; Xu et al. 2015; Chen et al. 2019). Recently, Han et al. (2019b, a) established a seasonal prediction model for summer rainfall amount and extreme rainfall frequency using preceding soil moisture over central Asia and SST in the tropical Atlantic Ocean.

Previous studies have also documented the impacts of Arctic signals on climate variation in NEC (Wu et al. 2008; He 2015; Gao et al. 2015). Specifically, both the Arctic sea ice extent and thickness show significant downward trends (Serreze et al. 2007; Serreze and Meier 2019), which has already exerted substantial impacts on climate and weather throughout the Northern Hemisphere through modulating surface heating and atmospheric circulation anomalies (Johannessen et al. 2004; Budikova 2009; Li and Wang 2014; Gimeno et al. 2019). The recent shrinkage of Arctic sea ice plays a critical role in recent cold and snow-rich winters in Europe and United States (Liu et al. 2012). Specifically, the sea-ice loss in Barents-Kara seas are followed by a colder Siberia and extreme cold events at northern continents (Petoukhov and Semenov 2010; Zhang et al. 2018). Wu et al. (2013) found a significant leading relationship between winter sea ice at west of Greenland and summer atmospheric circulation and rainfall anomalies over Eurasia. Moreover, recent publications have addressed the potential casual links between the sea ice anomalies and surface temperature anomalies (Li et al. 2015), haze days (Wang et al. 2015) and rainfall anomalies (Wu et al. 2009; Liu et al. 2019) over China. Han et al. (2015) suggested that the changes in Arctic sea ice contribute to the decadal decrease of rainfall at NEC after the late 1990s.

Recently, the influence of sea ice conditions in the Barents/Kara Sea on climate anomalies over China has received much attention (Li et al. 2014; Lin and Li 2018; Liu et al. 2019). Kug et al. (2015) stated that severe winters over East Asia are related to anomalous warmth in the Barents-Kara Sea region. Fan et al. (2018) noted that winter sea ice variability in Barents Sea is highly linked with spring dust activity in North China via the snow cover over western Siberia. He et al. (2018) identified the connection between the June sea ice variability in Barents Sea with the August triple rainfall pattern over eastern China. The diminishment in sea ice anomaly in Barents Sea lead to a decreased of snow depth over West Eurasia, which could affect the atmospheric circulation and soil moisture over the Yangtze River region and North China and further modulates summer hot drought events at NEC on the interannual timescale (Li et al. 2018). Therefore, intensive scientific interest is prompted in

possible linkage between the preceding sea ice area in Barents Sea and summer rainfall over NEC, which may provide useful information for the prediction and understanding of summer rainfall over NEC.

Midsummer rainfall at NEC exhibits regional homogeneity and south-north inverse pattern, which are affected by different circulation regimes (Han et al. 2019b, a). Previous studies focuses mostly on regional mean rainfall within NEC, whereas few refer to the south-north inverse pattern. Therefore, the primary goal of this study is to explore the potential relationship between sea ice area in Barents Sea and the south-north dipole pattern of midsummer rainfall over NEC, i.e. the second empirical orthogonal function (EOF2) mode of midsummer rainfall.

The rest of this paper is organized as follows. Section 2 introduces the datasets and methods used in the present study. Details of the relationship between sea ice in the Barents Sea and the EOF2 mode of NEC rainfall and the possible underlying mechanisms are described in Sect. 3. Finally, brief conclusions are presented in Sect. 4.

2 Data and methods

The monthly global atmospheric reanalysis products are derived from the National Centers for Environmental Prediction/National Center for Atmospheric Research for 1948–2016, with a horizontal resolution of $2.5^\circ \times 2.5^\circ$ (Kalnay et al. 1996). Variables used in this study include sea level pressure (SLP), horizontal wind (UV), geopotential height (Z), specific humidity, and vertical motion. The monthly sea ice concentration data and monthly SST data are provided by the Met Office Hadley Centre for 1870–2016, on a $1.0^\circ \times 1.0^\circ$ grid (Rayner et al. 2003). The sea ice area is used in this study, which is calculated as the product of sea ice concentration and the corresponding grid area.

An advanced daily rainfall observation dataset on a $0.25^\circ \times 0.25^\circ$ latitude-longitude grid (i.e. CN05.1), is used in the present study for the period 1961–2016 (Wu and Gao 2013). This dataset is constructed by interpolating data from over 2400 meteorological stations in China. NEC is defined as the region north of 38°N and east of 115°E in China. Midsummer rainfall is calculated as the summation of daily precipitation amounts from 1 July to 31 August annually. The EOF2 are obtained by performing EOF analysis on NEC midsummer rainfall (Fig. S1), and the corresponding principal component (i.e. PC2) is used to describe the interannual variation of this mode.

To further interpret the observational results, we conducted simulations with the National Center for Atmospheric Research Community Atmosphere Model, version 6, with a $0.9^\circ \times 1.25^\circ$ finite volume grid, and with 32 hybrid sigma pressure levels. The SST and sea ice

concentration are specified as boundary conditions based on a merged product of Reynolds/HADISST dataset (Hurrell et al. 2008).

In this study, early spring is defined as the mean for the months of March and April (MA), and early summer is calculated as the average during May and June (MJ). Midsummer refers to the average for July and August (JA). The common time period spans from 1961 to 2016. Regression, correlation, and composite analyses are conducted to investigate the atmospheric circulation anomalies associated with the NEC rainfall and sea ice in the Barents Sea. The Student's *t*-test is used to determine statistical significance. Additionally, linear trends are eliminated before analysis.

3 Results

3.1 Influence of early spring sea ice area in Barents Sea on the EOF2 mode of midsummer rainfall at NEC

The EOF2 mode of midsummer rainfall at NEC exhibits a south-north dipole structure, along with the greatest anomalies over the northern part (Fig. S1). The time series corresponding to this mode depicts the fluctuation of the dipole rainfall pattern, which are referred to as PC2. Figure 1a shows the correlation map between the PC2 and Arctic sea ice area during preceding early spring. Significant positive correlation coefficients are observed over the Barents Sea. Additionally, such positive correlations can be maintained continuously to summer (figures not shown). To

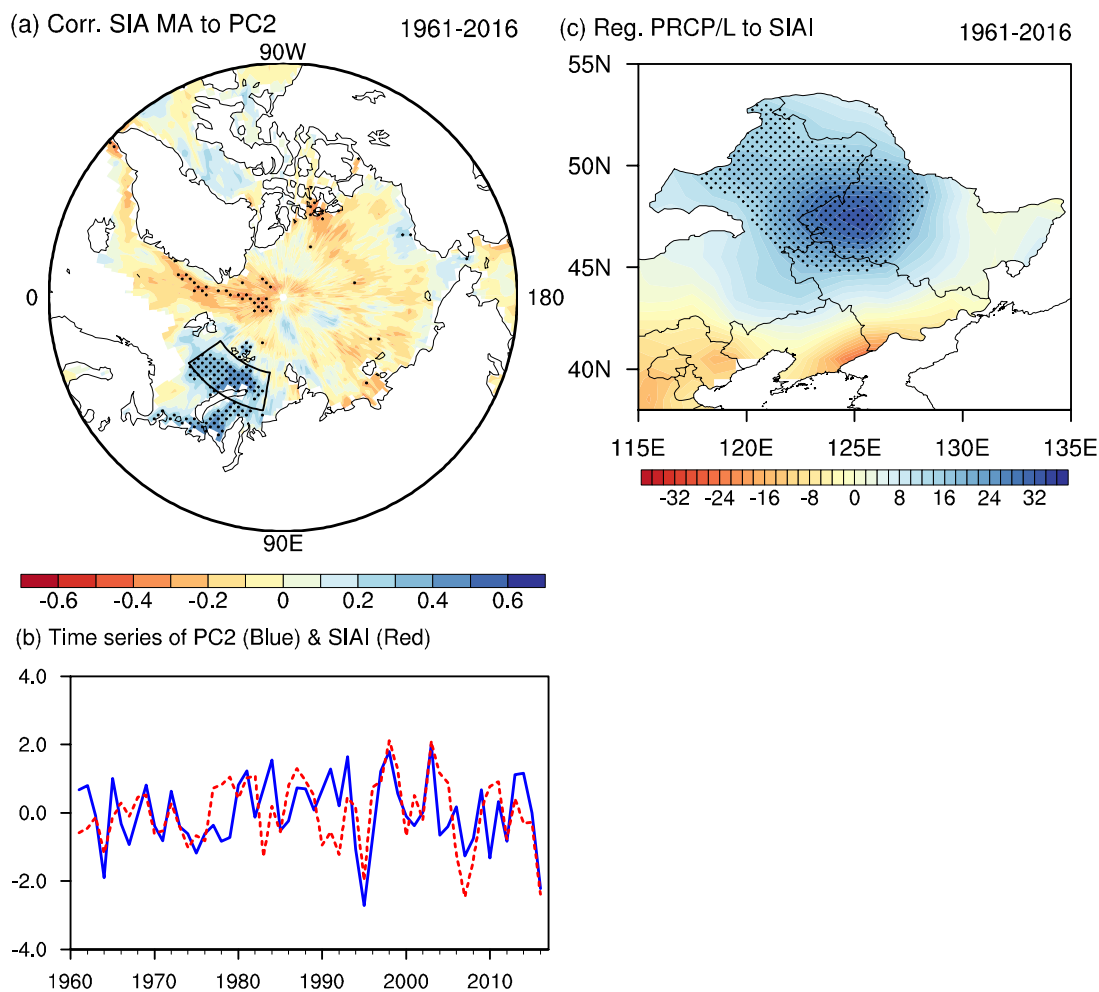


Fig. 1 **a** Correlation map of early spring sea ice area and the time series corresponding to the second principal component of midsummer rainfall at Northeast China (PC2) during 1961–2016. The black rectangular area in **(a)** represents the selected region for the sea ice area index (75°–80°N, 35°–80°E; SIAI). **b** Time series of the PC2

index (blue solid line) and SIAI over the Barents Sea (red dotted line). **c** Linear regression pattern of midsummer rainfall (unit: mm) against the SIAI index during 1961–2016. Stippling areas indicate the values that significantly exceed the 95% confidence level, estimated using Student's *t*-test

facilitate analysis, a sea ice area index (SIAI) is defined as the weighted area-averaged sea ice area during early spring over the Barents Sea (75° – 80° N, 35° – 80° E; as shown by the rectangle in Fig. 1a). As shown in Fig. 1b, the PC2 and SIAI indices are consistently in phase throughout the last five decades. The correlation coefficient between the two indices is 0.50 for 1961–2016, significant at the 99% confidence level. Specifically, increased sea ice area anomalies in the Barents Sea are followed by profound positive rainfall anomalies in the north and negative anomalies in the south of NEC during midsummer, along with large values over the northern part (Fig. 1c).

To further illustrate the effect of early spring sea ice anomalies over the Barents Sea on midsummer rainfall pattern at NEC, the atmospheric circulation anomalies related to the SIAI are examined. Generally, the SIAI-associated large-scale circulation displays a barotropic structure over the Eurasian continent, with similar pressure and height anomalies patterns near the surface and in the middle troposphere. Increased sea ice anomalies in the Barents Sea are characterized by dominant anomalous positive height and

anticyclonic winds over eastern Arctic, along with respective cyclone and anticyclone centered over Europe and Mediterranean Sea, displaying a meridional tripole pattern (Fig. 2a, b). Weak cyclonic and anticyclonic anomalies occupy Northwest and Southwest Siberia, respectively. Anomalous anticyclonic wind fields stretch zonally from Europe to East Asia over mid-latitudes, which can be seen at the middle and high levels (Fig. 2b, c). Moreover, an anomalous cyclone dominates Northeast China and adjacent regions. Han et al. (2019b, a) documented that the anticyclone or cyclone centered over NEC impacts substantially on the EOF2 mode of midsummer rainfall. It is apparent that southeasterly anomaly prevails at the northern and eastern NEC, and northwesterly anomaly emerges at the western and southern portion. Accordingly, predominant moisture convergence anomalies are centered over southern Japan Islands (Fig. 2d). The peripheral southeasterly or easterly current at the northern flank transport water vapor from the Northwest Pacific to the eastern and northern NEC across the eastern boundary, inducing conspicuous convergence anomalies of moisture. In addition, anomalous northerly flow leads to prominent

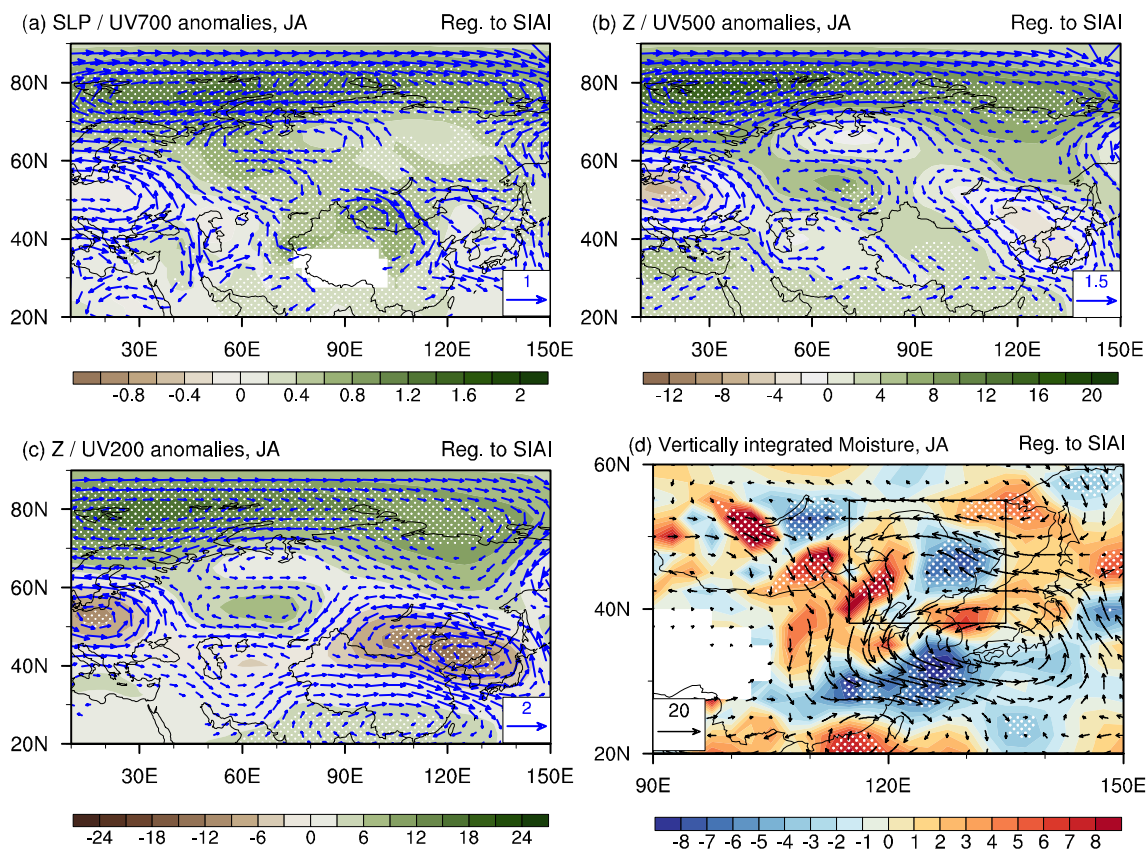


Fig. 2 Linear regression pattern of midsummer **a** sea level pressure (SLP; unit: mb; shaded) and 700 hPa horizontal wind (unit: m s^{-1} ; vectors), **b** 500 hPa geopotential height (unit: m; shaded) and horizontal wind (unit: m s^{-1} ; vectors), **c** 200 hPa geopotential height (unit: m; shaded) and horizontal wind (unit: m s^{-1} ; vectors), and **d**

vertically integrated water vapor transport ($\text{kg m}^{-1} \text{s}^{-1}$; vectors) and divergence ($10^{-6} \text{kg m}^{-2} \text{s}^{-1}$; shaded) with regard to the SIAI during 1961–2016. Stippling areas indicate the values that significantly exceed the 90% confidence level, estimated using Student's *t*-test. Vectors greater than 0.2m s^{-1} are plotted

divergence anomalies of moisture over the western and southern part. These atmospheric circulation and moisture conditions during midsummer following increased sea ice during early spring over the Barents Sea are favorable (unfavorable) for rainfall over the north (south) of NEC.

Dynamic processes are also essential for rainfall distribution. Figure 3a, b present the linear regression of divergence and vertical movement anomalies in following midsummer related to the early spring SIAI. Corresponding to increased sea ice in the Barents Sea, significant convergence and divergence anomalies appear in the lower-to-middle and upper troposphere over the northern NEC (i.e., north of 42°N), respectively, which further trigger ascending motion based on the continuity equation. At the south of NEC, the lower-level divergence and upper-level convergence excites anomalous descending movement. Enhanced water vapor content and upward motion anomalies induce increased total cloud cover in the northern part through condensation, whereas reduced moisture transport and downward motion lead to

decreased total cloud cover (Fig. 3c). Consistently, precipitable water content is intensified in the northern part but lessened at the south (Fig. 3d).

These above results show that the increased early spring sea ice area in the Barents Sea can cause a meridional tri-pole pattern of atmospheric circulation anomalies over the region from eastern Arctic to Mediterranean Sea. An anomalous cyclone emerges over NEC and moisture convergence anomaly is centered over the southern Japan, along with the dominance of anomalous southeasterly at the northern and eastern NEC and of anomalous northerly at the western and southern part. Consequently, anomalous convergence (divergence) of water vapor occupies the north (south) of NEC. Moreover, the upper-level divergence (convergence) and lower-level convergence (divergence) anomalies lead to ascending (descending) movement and further increased (decreased) total cloud cover over the northern (southern) part. These conditions jointly facilitate to enhance (reduce) rainfall anomalies at the north (south) of NEC.

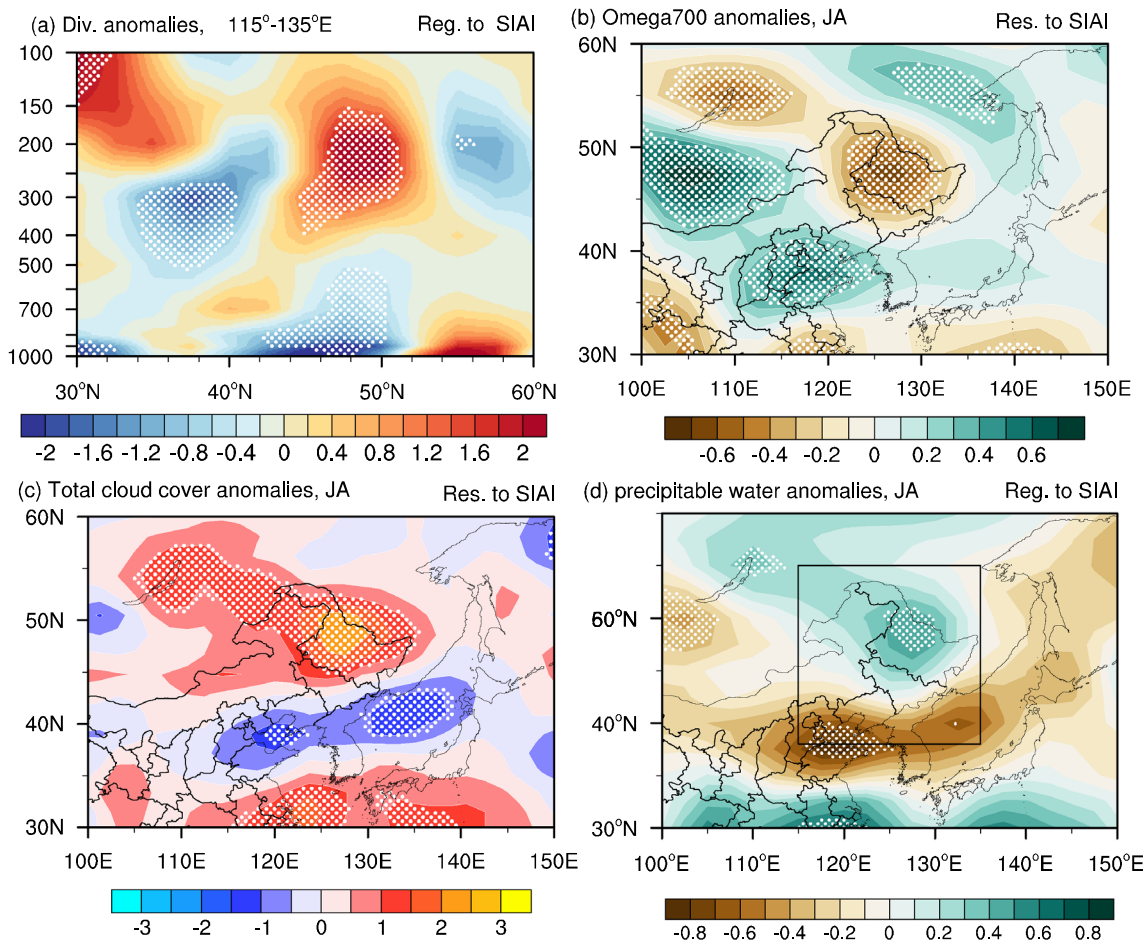


Fig. 3 a Vertical–horizontal cross section averaged within (115° – 135° E) for divergence anomalies (unit: 10^{-7} Pa) during midsummer regressed onto the SIAI during 1961–2016. Linear regression pattern of midsummer b vertical motion at 700 hPa (unit: 10^{-2} Pa s^{-1}), c

total cloud cover (unit: %) and d precipitation water content (unit: $kg\ m^{-2}$) against the SIAI during 1961–2016. Stippling areas indicate the values that significantly exceed the 90% confidence level, estimated using Student's *t*-test

3.2 Possible mechanisms

Previous studies have shown remarkable regional and inter-annual variation in Arctic sea ice (Parkinson et al. 1999; Wei et al. 2019). Generally, the average seasonal cycle of sea ice area in the Barents Sea reaches maximum during early spring, with the largest value in April (Fig. S1). As presented in Fig. 4, the anomalies of sea ice area at Barents Sea have a good seasonal persistence from early spring to midsummer, despite of small western shrinkage during summer. Accordingly, two sea ice area indices, named SIA MJ and SIA JA, respectively, are defined by averaging sea ice area over the Barents Sea during early summer and midsummer. The correlation coefficient (shorted as CC) between SIA MA and SIA MJ indices is 0.75 for 1961–2016, the CC between SIA MA and SIA JA indices is 0.42, and the CC between SIA MJ and SIA JA indices is 0.65 (all significant at the 99% confidence level). Therefore, the sea ice anomalies over the Barents Sea are maintained well from early spring to summer, which could exert a prolonged impact on the midsummer circulation anomalies over Eurasian continent and further rainfall distribution over NEC.

Tetzlaff et al. (2013) determined that up to 70–90 % of near-surface air temperature variance over the Arctic Ocean during winter and spring is explained by the distribution of surface temperature along the air mass trajectory, which is mostly controlled by sea ice. During early spring, the expected direct local influence of increased sea ice area anomalies is the reduced upward turbulent heat net flux of sensible and latent heat from the ocean to the atmosphere (Fig. 5a), which consequently has a cooling effect on near-surface air temperature in situ (Fig. 5b). Cooling air temperature anomalies is also dominant over Barents Sea during summer due to the persistence of sea ice area anomalies (Fig. 5c), which further increases the vertical static stability. Accordingly, prominent descending motion anomalies

emerge over the Barents Sea due to the changes in thermal forcing (Fig. 5d). It further triggers anomalous ascending, descending and ascending movement meridionally extending from North Europe to Mediterranean Sea, which may be attributed to meridional vertical cells (Figs. 2 and 6a). Moreover, alternation of upward and downward anomalies orients zonally from Mediterranean Sea to East Asia (Figs. 5d and 6b), and exhibit a barotropic structure throughout the troposphere at mid-latitudes (Fig. 6b), which resembles the Silk Road Pattern (SRP). In addition, alternative anomalies of descent and ascent extend over Barents Sea, Siberia, Northeast Asia, and northern NEC, which exhibits a southeastward-oriented wavelike pattern.

The SRP, initially proposed by Lu et al. (2002), is a teleconnection pattern trapped along Asian westerly jet stream in the upper troposphere during summer. Previous studies have demonstrated that the SRP is originated from the eastern Mediterranean and Caspian Sea (Yasui and Watanabe 2010; Chen and Huang 2012). To explore the potential effect of sea ice anomalies on the formation of the SRP, the anomalous upper-level divergence and Rossby wave source (RWS) associated with SIA JA index are investigated. As shown in Fig. 6c, the remarkable feature is the predominant divergence and RWS anomalies over eastern Mediterranean Sea at upper layer in response to increased sea ice area anomalies in the Barents Sea. Sardeshmukh and Hoskins (1988) proposed that the advection of vorticity by divergence wind can act as a wave source. The Barents sea ice area anomaly could affect vertical motion anomaly over the Mediterranean Sea through the meridional vertical cells (Figs. 5d and 6a), and then induce divergence anomalies in the high troposphere. The RWS anomalies are well concurrent with where the anomalous divergence is located. Consistent results are also detectable in composite analysis (figure not shown). Furthermore, the first EOF mode of meridional wind at 200 hPa (V200) is extensively used to describe the Silk Road

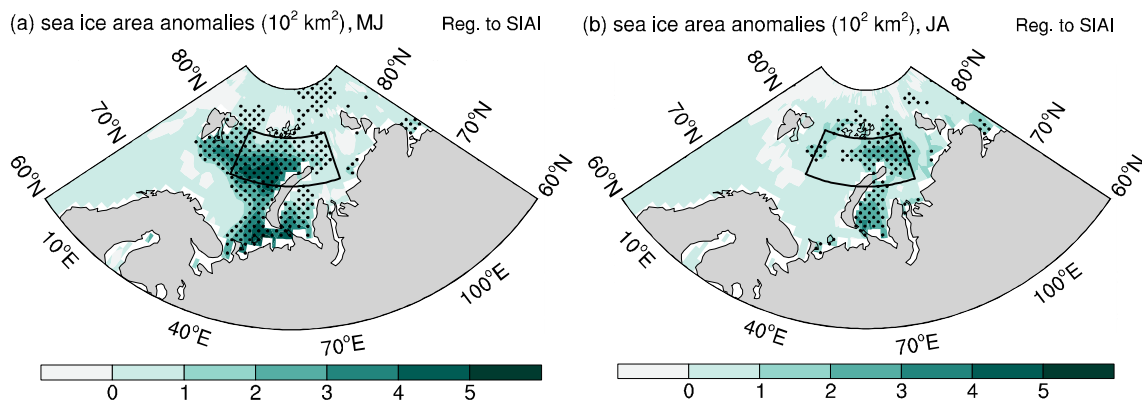


Fig. 4 Linear regression pattern of sea ice area during **a** early summer, **b** midsummer (unit: 10^2 km^2) against the SIAI during 1961–2016. The black rectangular area in **b** represents the selected region

for the sea ice area index during midsummer (SIA JA). Stippling areas indicate the values that significantly exceed the 95% confidence level, estimated using Student's *t*-test

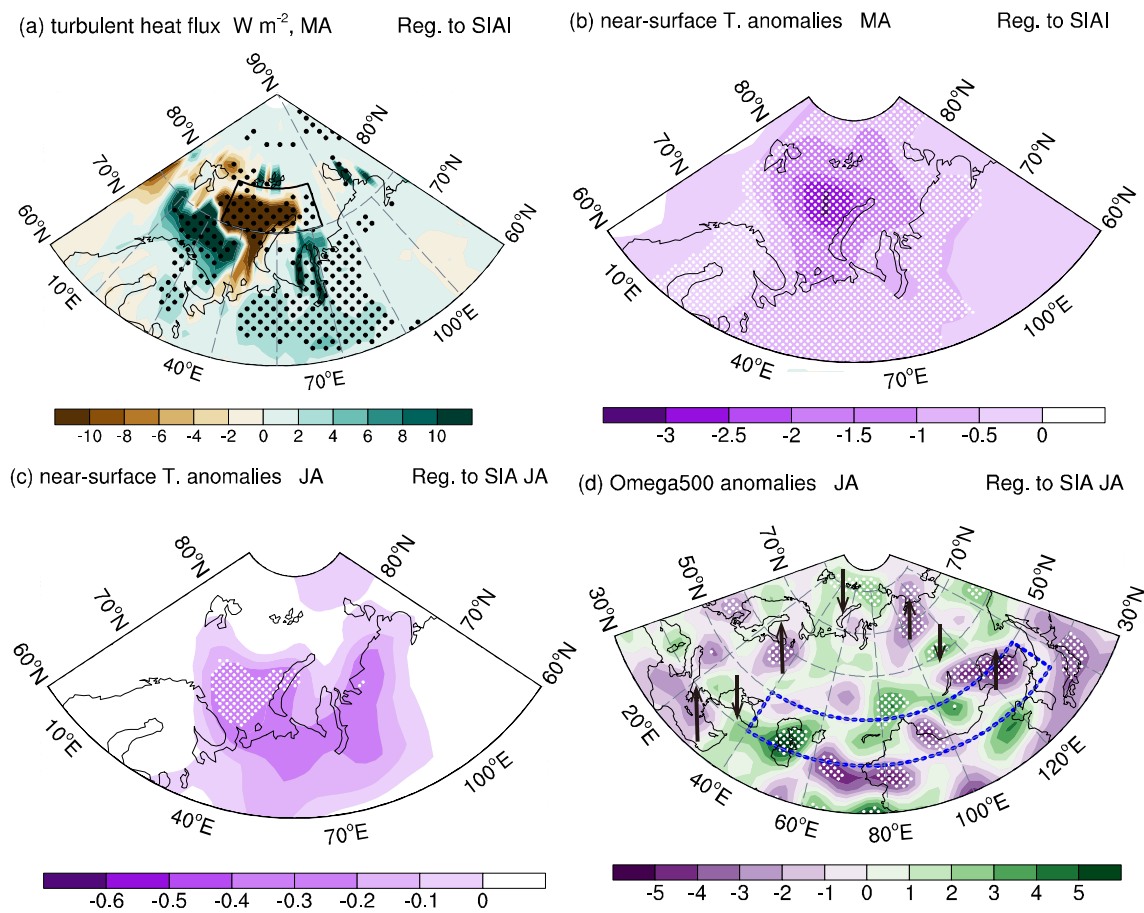


Fig. 5 Linear regression pattern of **a** total turbulent heat flux (sensible plus latent heat flux; unit: W m^{-2}), and **b** air temperature at sigma level 0.995 during early spring (unit: degC) against the SIAI. Linear regression pattern of midsummer **c** air temperature at sigma level

0.995 (unit: degC), and **d** 500 hPa vertical movement ($10^{-2} \text{ Pa s}^{-1}$) against the SIA JA index during 1961–2016. Stippling areas indicate the values that significantly exceed the 90% confidence level, estimated using Student's *t*-test

Pattern (Kosaka et al. 2009; Yasui and Watanabe 2010; Chen and Huang 2012). Consequently, the EOF analysis is performed on V200 within the domain (30° – 60°N , 10° – 130°E), and the Silk Road Pattern index (SRPI) is defined as the standardized time series corresponding to the first EOF mode. The first EOF mode of V200 accounts for 35.1% of the total variance. This SRP index is highly correlated with the indices defined in previous studies. For example, the correlation coefficients between SRPI with those defined by Kosaka et al. (2009) and Chen and Huang (2012) are both 0.99 for 1961–2016. As shown in Fig. 6d, the SRP is associated with prominent RWS and divergence anomalies over eastern Mediterranean Sea, and the SIA JA-associated RWS anomalies are similar to the counterparts related with SRP.

The Asian westerly jet stream can act as a waveguide in the upper troposphere (Hoskins and Ambrizz 1993). As mentioned before, increased sea ice anomalies in the Barents Sea are characterized by anomalous cyclones stretching zonally at the mid-latitudes of Eurasia at the upper layer (Fig. 2c). Consistently, notable easterly anomalies appear at

the mid-to-high latitudes of East Asia and westerly anomalies occur at the midlatitudes (Fig. 7a). The easterly anomaly over northern NEC and westerly anomaly over the Northwest Pacific are accordant with the anomalous cyclone over NEC (Fig. 2). These results are consistent with Hong and Lu (2016) who documented that the meridional displacement of the Asian westerly jet stream is significantly linked with the Silk Road Pattern. They identified that when the Asian jet is in southward shift, the Silk Road Pattern is accompanied by cyclonic anomalies over East Asia. To illustrate the relationship between the Silk Road Pattern and sea ice anomalies in the Barents Sea, the linear regression of the upper-level meridional wind and wave activity flux (WAF) anomalies with regard to the SIA JA index are further investigated (Fig. 7b). The WAF is calculated according to Plumb's formulation (Plumb 1985) and it can depict the propagation of stationary Rossby waves. It is visible that a Rossby wave train propagates in a polar route at high latitudes; having originated in Barents Sea, it then diffuses southeastward to Northeast Asia and NEC. This wave pattern could also

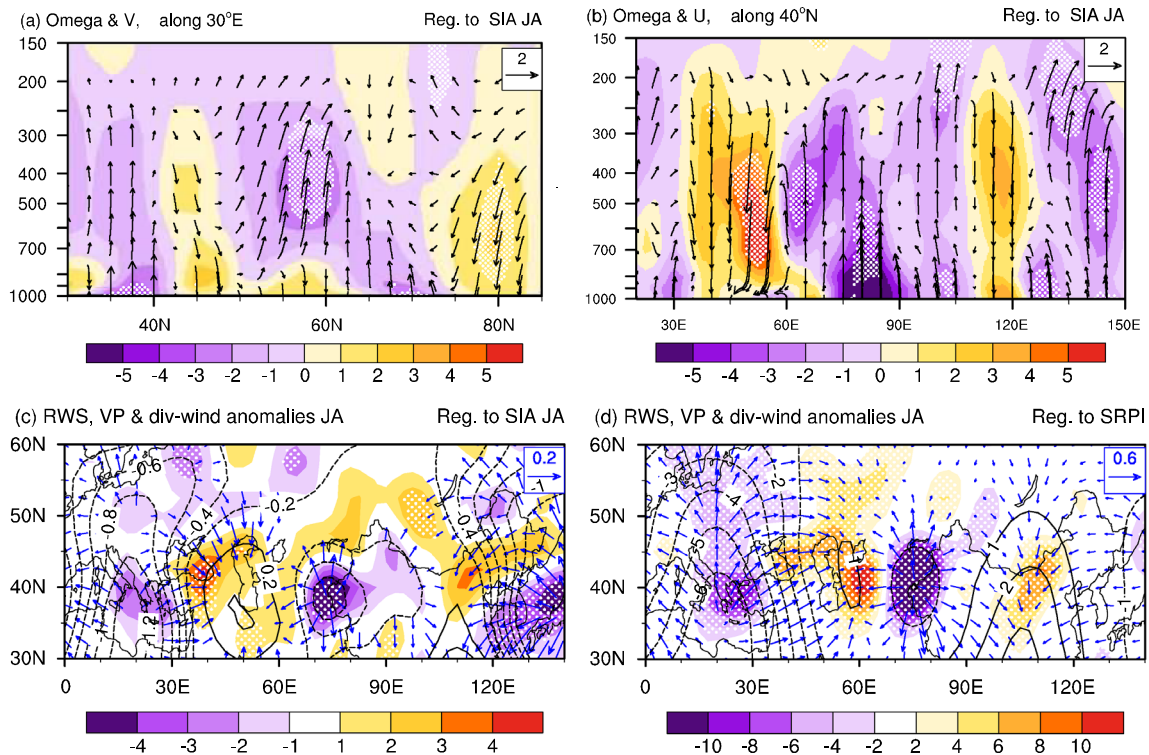


Fig. 6 Vertical-horizontal cross section for midsummer vertical wind (unit: m s^{-1} ; vectors) and omega (unit: $-10^{-3} \text{ Pa s}^{-1}$; shaded) anomalies along **a** 30°E , and **b** 40°N regressed onto the SIA JA index during midsummer for 1961–2016. Linear regression pattern of 200 hPa velocity potential (unit: $10^5 \text{ m}^2 \text{ s}^{-1}$; contours), divergent horizontal wind (unit: m s^{-1} ; vectors), and Rossby wave source (unit: 10^{-11} s^{-2} ;

shaded) during midsummer against **c** the SIA JA index and **d** the Silk Road Pattern index during 1961–2016. The Silk Road Pattern index is defined as the time series corresponding to the first EOF mode of meridional wind at 200 hPa during midsummer within the domain ($30^\circ\text{--}60^\circ\text{N}$, $10^\circ\text{--}130^\circ\text{E}$)

be recognized in the associated meridional wind anomaly fields. More important, there are alternations of southerly and northerly anomalies extending from the eastern to northern China at mid-latitudes, which agree well with the SRP structure (Fig. 7c). The pattern correlation coefficient is 0.83 between Fig. 7b, c for the meridional wind anomalies within the mid-latitudes of Eurasia ($30^\circ\text{--}60^\circ\text{N}$, $10^\circ\text{--}130^\circ\text{E}$). In addition, in response to sea ice anomalies, a conspicuous Rossby wave train propagates eastward to East Asia along the Asian western jet stream (Fig. 7b), confirming that the zonally oriented Rossby wave pattern at midlatitudes is closely linked with sea ice anomalies over the Barents Sea.

These results imply that the sea ice area anomaly in the Barents Sea has a good seasonal persistence from spring to summer, and that it could affect air temperature and vertical movement anomalies in situ via modulating turbulence heat net flux. The vertical motion and divergence anomalies are further triggered over Europe and Mediterranean Sea through the meridional vertical cells. The advection of vorticity by divergence wind acts as an effective Rossby wave source over eastern Mediterranean Sea. Therefore, the Silk

Road Pattern propagates eastward to East Asia along the Asian westerly jet stream, by which the sea ice anomalies in the Barents Sea affect midsummer rainfall pattern over NEC by the modulation on atmospheric circulation anomalies. In addition, another Rossby wave train, originated in Barents Sea, diffuses directly southeastward to Northeast Asia and NEC in a polar path.

3.3 Numerical simulations

The impact of sea ice anomalies in the Barents Sea on rainfall distribution over NEC is assessed by comparing two experiments with different seasonally varying sea ice concentration and SST, and all other external variables are fixed. The control experiment is run with seasonal varying climatology (1995–2005) of sea ice concentration and SST (Hurrell et al. 2008). The perturbed experiment is similar to the control experiment, but superposed with sea ice concentration and SST anomalies during March to August over the Barents Sea ($75^\circ\text{--}80^\circ\text{N}$, $35^\circ\text{--}80^\circ\text{E}$; Figs. 8 and 9). The sea ice concentration and SST anomalies are calculated as

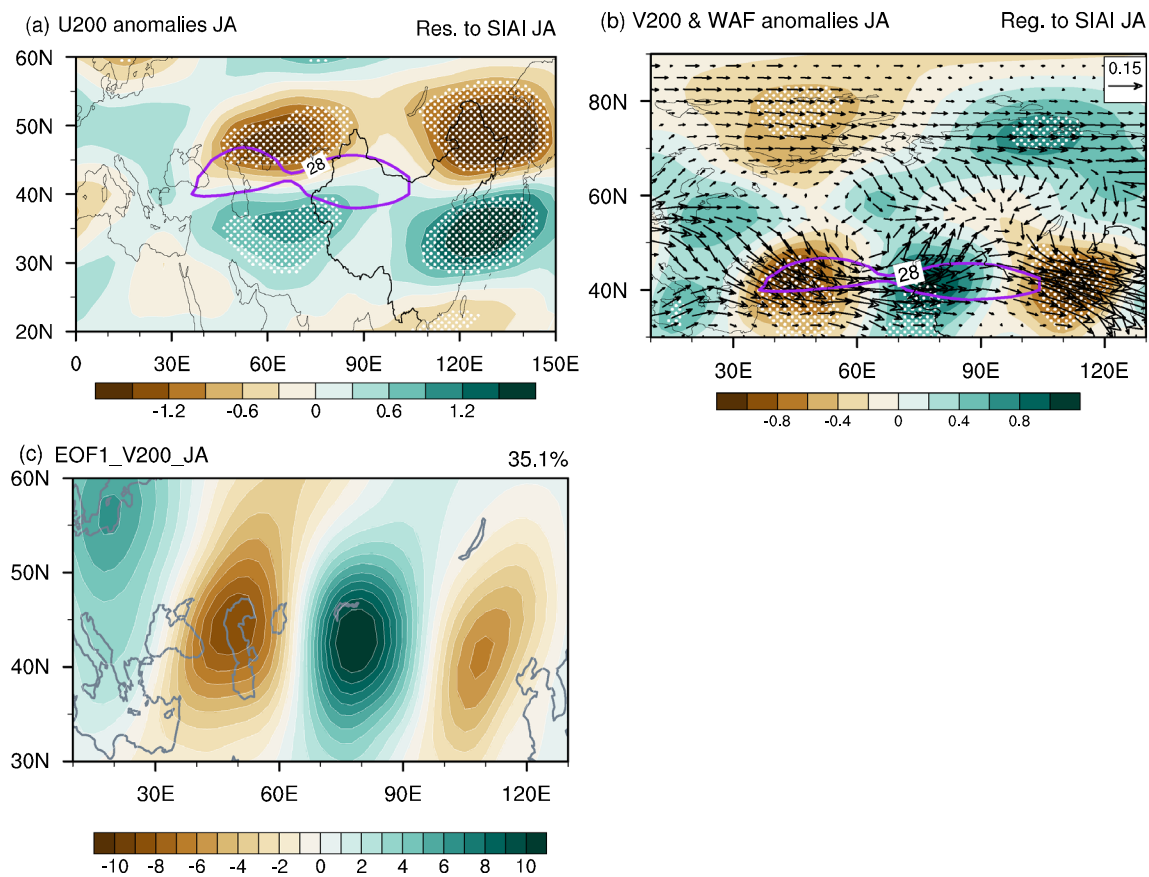


Fig. 7 Linear regression pattern of 200 hPa **a** zonal wind (unit: m s^{-1}), and **b** meridional wind (unit: m s^{-1} ; shaded) and wave activity flux (unit: $\text{m}^2 \text{s}^{-2}$; vectors) during midsummer against the SIAI JA index during 1961–2016. The purple line is the climatology of zonal

wind with a value of 28 m s^{-1} . Stippling areas indicate the values that significantly exceed the 90% confidence level, estimated using Student's *t*-test. **c** The first EOF mode for midsummer meridional wind at 200 hPa in the domain ($30^\circ\text{--}60^\circ\text{N}$, $10^\circ\text{--}130^\circ\text{E}$)

the differences between positive and negative SIAI years. These years are selected characterized by the absolute of SIAI index greater than 1 (Table 1). Increases sea ice anomalies are generally accompanied by cooling SST anomalies in Barents Sea, together with a good seasonal persistence of sea ice and SST anomalies from spring to summer. Each run is integrated for 9 years, and the results for the last 5 years are analyzed. We focused on the differences between the perturbed and control experiments during midsummer to examine response of atmospheric circulation to the sea ice anomalies over the Barents Sea.

As shown in Fig. 10a, b, increased sea ice over the Barents Sea does induce positive SLP and height anomalies over high latitudes and negative anomalies over further south during midsummer, which is accompanied by anticyclonic wind anomalies over eastern Arctic and cyclonic anomalies at mid-latitudes. Moreover, moisture convergence

is found over NEC, along with anomalous convergence of moisture over northern and eastern NEC and with divergence over western and southern part (Fig. 10c). The divergence wind and Rossby wave source anomalies are also detected over eastern Mediterranean Sea in model simulation (Fig. 10d). While the regional details differ somewhat between the response of the modeled circulation and the observation, the model simulation does show above-normal midsummer precipitation, total cloud cover, precipitable water content and ascending motion in north of NEC, and below-normal midsummer precipitation, total cloud cover, precipitable water content and descending motion in south (Fig. 11). The encouraging consistency between model simulations and observations supports our hypothesis that sea ice anomalies over the Barents Sea during early spring tend to induce dipole rainfall pattern over NEC in the ensuing midsummer.

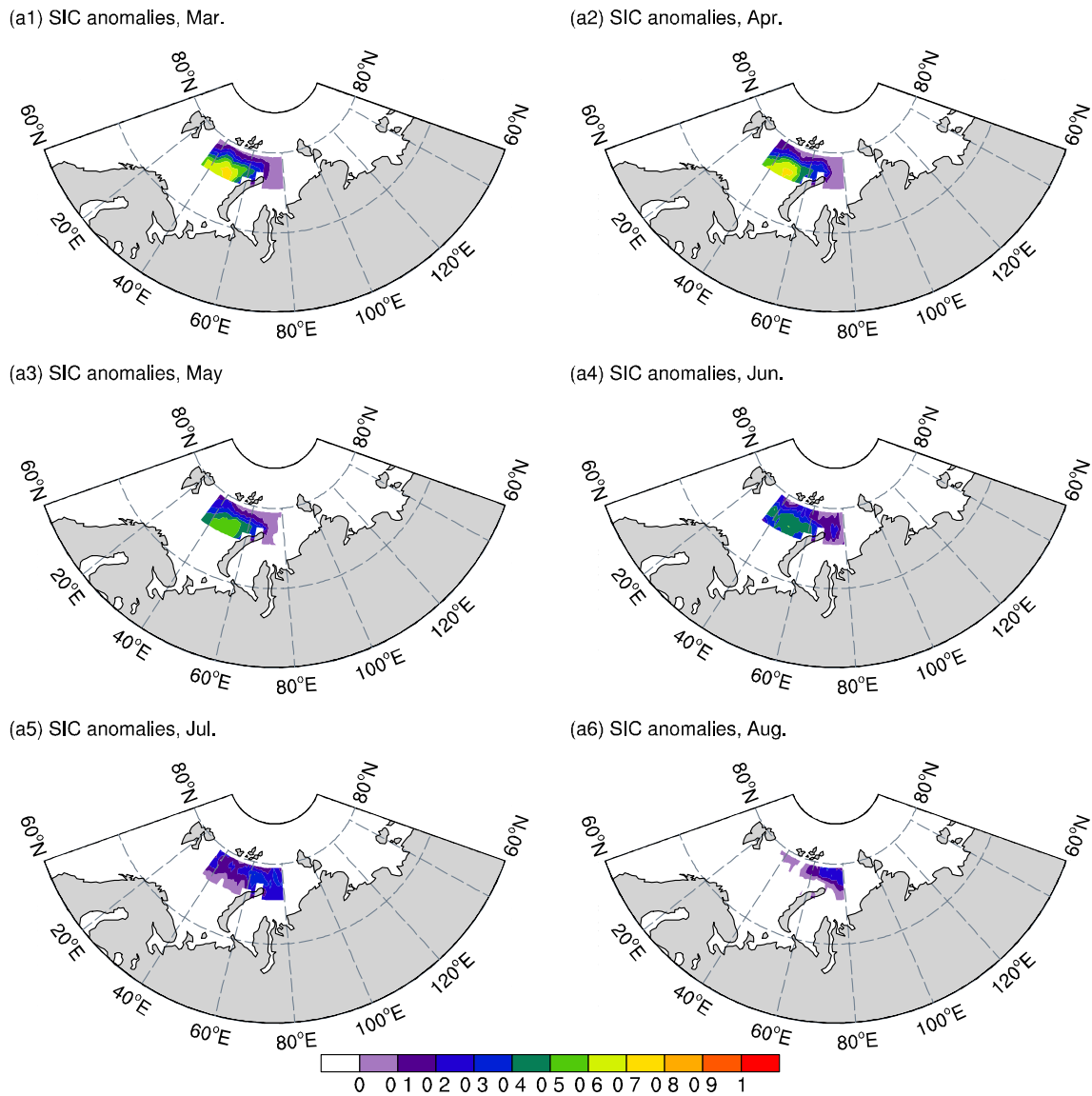


Fig. 8 Differences of sea ice concentration between the positive and negative SIAI years during March to August. The positive (negative) SIAI years are selected characterized by SIAI greater (less) than 1 (−1)

4 Conclusion

This study documents the influence of early spring sea ice anomalies over the Barents Sea on the dipole rainfall pattern over Northeast China during the ensuing midsummer. Increased sea ice area in the Barents Sea is followed

by increased rainfall anomalies at north of NEC as well as by decreased anomalies at south, and vice versa. The sea ice anomalies over the Barents Sea can be maintained well from spring to summer, and induce near-surface air temperature and vertical movement anomalies in situ via modulating turbulent heat net flux. The circulation

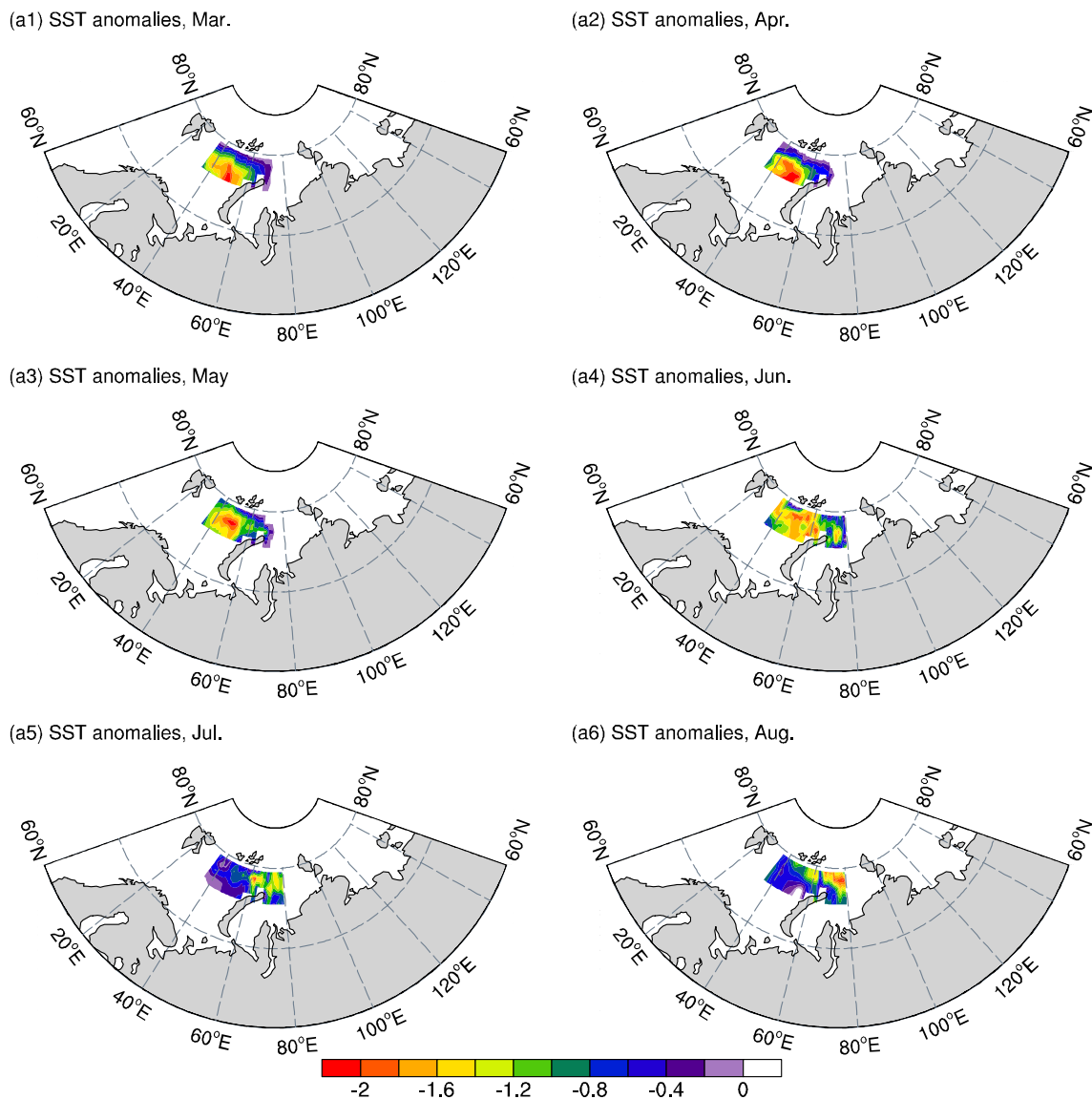


Fig. 9 Same as Fig. 8, but for SST

Table 1 Years characterized by the absolute of SIAI index greater than 1 during 1961–2016

Category	Years
SIAI > 1	1979, 1981, 1982, 1987, 1998, 1999, 2003, 2004
SIAI < -1	1964, 1974, 1983, 1992, 1995, 2006, 2007, 2008, 2016

anomalies could be triggered over Europe and Mediterranean Sea through the meridional vertical circulation. Furthermore, a Rossby wave source is excited over eastern Mediterranean Sea by the advection of vorticity by divergence wind. Accordingly, the Silk Road Pattern, originating from Mediterranean Sea, propagates eastward to East Asia along the Asian westerly jet stream. In addition, a relative weak wave-like train can diffuse directly southeastward from Arctic to NEC by a polar path. As a consequence, in response to increased sea ice anomalies at the Barents Sea, prominent cyclone anomalies occupy NEC, concurrent with anomalous moisture convergence

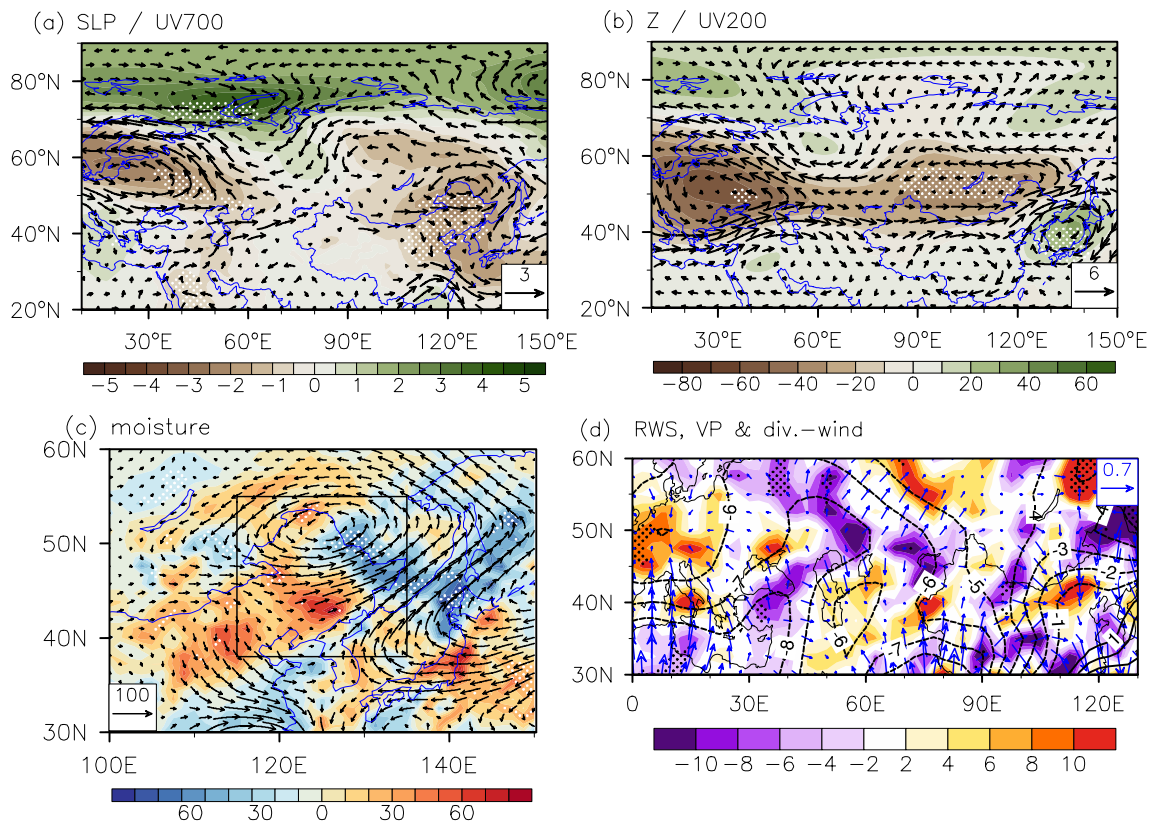


Fig. 10 The difference in **a** SLP (unit: mb; shaded) and 700 hPa horizontal wind (unit: m s^{-1} ; vectors), **b** geopotential height (unit: m; shaded) and horizontal wind (unit: m s^{-1} ; vectors) at 200 hPa, **c** vertically integrated water vapor transport ($\text{kg m}^{-1} \text{s}^{-1}$; vectors) and divergence ($10^{-6} \text{ kg m}^{-2} \text{s}^{-1}$; shaded), and **d** velocity potential ($10^5 \text{ m}^2 \text{s}^{-1}$;

contours), divergent horizontal wind (m s^{-1} ; vectors) and Rossby wave source (10^{-11} s^{-2} ; shaded) at 200 hPa between perturbed and control experiments. Stippling areas indicate the values that significantly exceed the 90% confidence level, estimated using Student's *t*-test

centered over southern Japan. The southeasterly anomalies over the north of NEC co-occur with convergence of moisture, and northerly anomalies over the south lead to divergence of moisture. In addition, the upper-level divergence and lower-level convergence occupy the northern NEC, inducing ascending anomalies; while the upper-level convergence and lower-level divergence appear over the southern part, causing descending anomalies. These

conditions jointly lead to increased total cloud cover and precipitable water content anomalies at north of NEC, and decreased total cloud cover and precipitable water content anomalies at the southern region. Numerical simulations support that sea ice anomalies over the Barents Sea during early spring tend to induce dipole rainfall pattern over NEC in the ensuing midsummer.

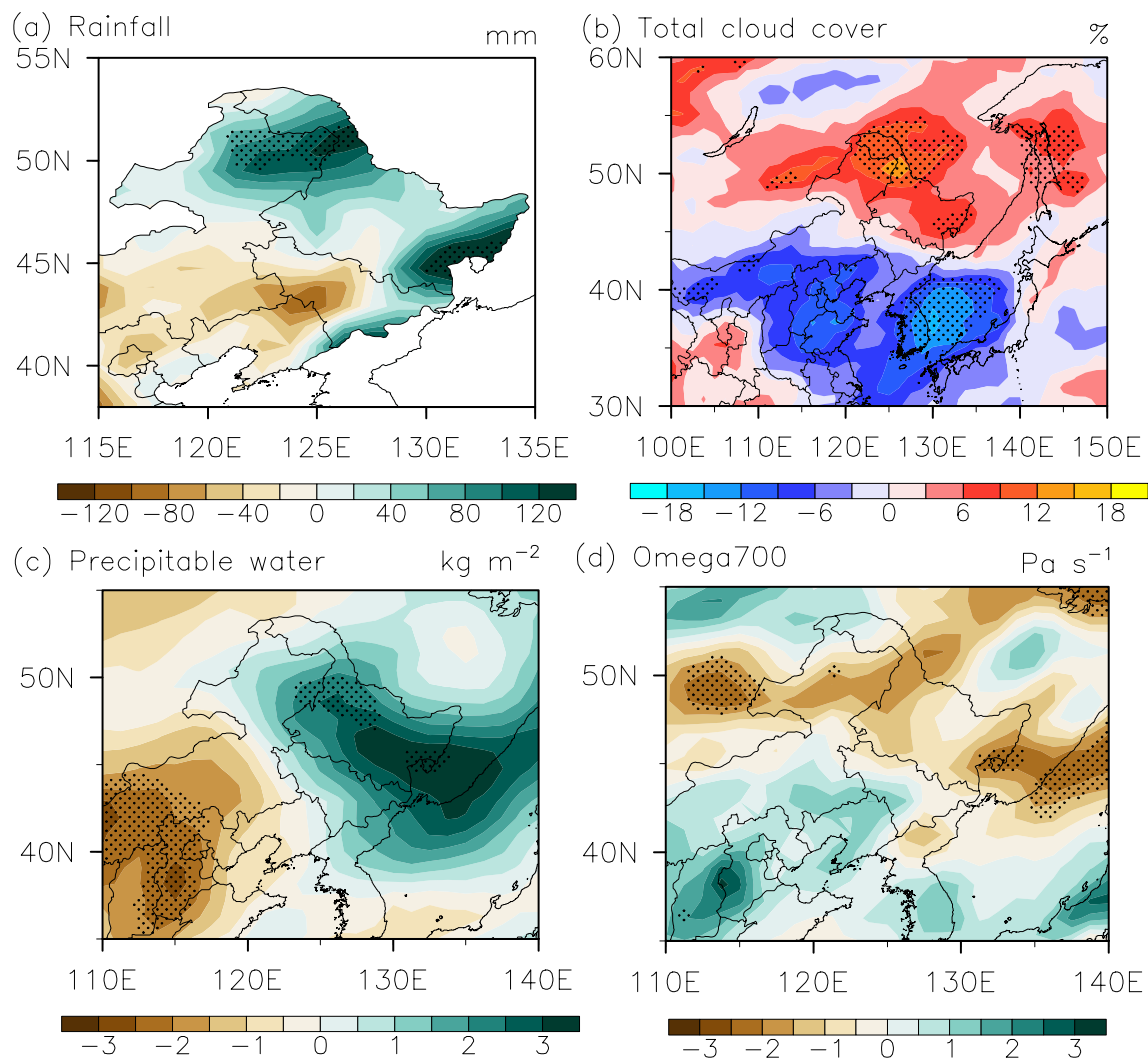


Fig. 11 The difference in **a** precipitation (unit: mm), **b** total cloud cover (unit: %), **c** precipitable water content (kg m^{-2}) and **d** vertical movement at 700 hPa ($10^{-2} \text{ Pa s}^{-1}$) between perturbed and control

experiments. Stippling areas indicate the values that significantly exceed the 90% confidence level, estimated using Student's *t*-test

Supplementary Information The online version contains supplementary material available at <https://doi.org/10.1007/s00382-021-05754-4>.

Acknowledgments This work was jointly supported by the National Natural Science Foundation of China (Grants Nos. 42025502, 41805046, 41875118 and 41875119).

References

- Budikova D (2009) Role of Arctic sea ice in global atmospheric circulation: a review. *Globe Planet Change* 68:149–163. <https://doi.org/10.1016/j.gloplacha.2009.04.001>
- Chen D, Sun JQ, Gao Y (2019) Distinct impact of the Pacific multi-decadal oscillation on precipitation in Northeast China during April in different Pacific multi-decadal oscillation phases. *Int J Climatol*. <https://doi.org/10.1002/joc.6291>
- Chen GS, Huang RH (2012) Excitation mechanisms of the teleconnection patterns affecting the July precipitation in northwest China. *J Clim* 25:7834–7851. <https://doi.org/10.1175/JCLI-D-11-00684.1>
- Fan K, Xie ZM, Wang HJ, Xu ZQ, Liu JP (2018) Frequency of spring dust weather in North China linked to sea ice variability in the Barents Sea. *Clim Dyn* 51:4439–4450. <https://doi.org/10.1007/s00382-016-3515-7>
- Gao YQ, Coauthors, (2015) Arctic sea ice and Eurasian climate: A review. *Adv Atmos Sci* 32:92–114. <https://doi.org/10.1007/s00376-014-0009-6>
- Gimeno L, Vázquez M, Eiras-Barca J, Sorí R, Algarra I, Nieto R (2019) Atmospheric moisture transport and the decline in Arctic Sea ice. *WIREs Clim Change* 10:e588. <https://doi.org/10.1002/wcc.588>

- Han TT, Chen HP, Wang HJ (2015) Recent changes in summer precipitation in Northeast China and the background circulation. *Int J Climatol* 35:4210–4219. <https://doi.org/10.1002/joc.4280>
- Han TT, He SP, Wang HJ, Hao X (2019a) Variation in principal modes of midsummer precipitation over Northeast China and its associated atmospheric circulation. *Adv Atmos Sci*. 36:55–64. <https://doi.org/10.1007/s00376-018-8072-z>
- Han TT, He SP, Wang HJ, Hao X (2018) Enhanced influence of early-spring tropical Indian Ocean SST on the following early-summer precipitation over Northeast China. *Clim Dyn* 51:4065–4076. <https://doi.org/10.1007/s00382-017-3669-y>
- Han TT, Wang HJ, Sun JQ (2017) Strengthened relationship between eastern ENSO and summer precipitation over Northeastern China. *J Clim* 30:4497–4512. <https://doi.org/10.1175/JCLI-D-16-0551.1>
- Han TT, Wang HJ, Hao X, Li SF (2019b) Seasonal prediction of midsummer extreme precipitation days over Northeast China. *J Appl Meteorol Climatol* 58:2033–2048. <https://doi.org/10.1175/JAMC-D-18-0253.1>
- He SP (2015) Asymmetry in the Arctic Oscillation teleconnection with January cold extremes in Northeast China. *Atmos Oceanic Sci Lett* 8:386–391. <https://doi.org/10.3878/AOSL20150053>
- He SP, Gao YQ, Furevik T, Wang HJ, Li F (2018) Teleconnection between sea ice in the Barents Sea in June and the Silk Road, Pacific-Japan and East Asian rainfall patterns in August. *Adv Atmos Sci* 35:52–64. <https://doi.org/10.1007/s00376-017-7029-y>
- Hong XW, Lu RY (2016) The meridional displacement of the summer Asian jet, silk road pattern, and tropical SST anomalies. *J Clim* 29:3753–3766. <https://doi.org/10.1175/JCLI-D-15-0541.1>
- Hoskins BJ, Ambrizzi T (1993) Rossby wave propagation on a realistic longitudinally varying flow. *J Atmos Sci* 50:1661–1671. [https://doi.org/10.1175/1520-0469\(1993\)050<1661:RWPOAR.2.0.CO;2](https://doi.org/10.1175/1520-0469(1993)050<1661:RWPOAR.2.0.CO;2)
- Hu KX, Lu RY, Wang DH (2010) Seasonal climatology of cut-off lows and associated precipitation patterns over Northeast China. *Meteor Atmos Phys* 106:37–48. <https://doi.org/10.1007/s00703-009-0049-0>
- Huang BY, Coauthors, (2017) Extended reconstructed sea surface temperature version 5 (ERSSTv5), Upgrades, validations, and intercomparisons. *J Clim* 30:8179–8205. <https://doi.org/10.1175/JCLI-D-16-0836.1>
- Hurrell JW, Hack JJ, Shea D, Caron JM, Rosinski J (2008) A new sea surface temperature and sea ice boundary dataset for the community atmosphere model. *J Clim* 21:5145–5153. <https://doi.org/10.1175/2008JCLI2292.1>
- Johannessen OM, Coauthors, (2004) Arctic climate change: observed and modelled temperature and sea-ice variability. *Tellus* 56A:328–341. <https://doi.org/10.3402/tellusa.v56i4.14418>
- Kalnay E, Coauthors, (1996) The NCEP/NCAR 40-year reanalysis project. *Bull Amer Meteorol Soc* 77:437–471. [https://doi.org/10.1175/1520-0477\(1996\)077<3c0437:TNYRP%3e2.0.CO;2](https://doi.org/10.1175/1520-0477(1996)077<3c0437:TNYRP%3e2.0.CO;2)
- Kosaka Y, Nakamura H, Watanabe M, Kimoto M (2009) Analysis on the dynamics of a wave-like teleconnection pattern along the summertime Asian jet based on a reanalysis dataset and climate model simulations. *J Meteor Soc Japan* 87:561–580. <https://doi.org/10.2151/jmsj.87.561>
- Kug JS, Coauthors, (2015) Two distinct influences of Arctic warming on cold winters over North America and East Asia. *Nat Geosci* 8:759–762. <https://doi.org/10.1038/ngeo2517>
- Li F, Wang HJ, Gao YQ (2014) On the strengthened relationship between East Asian winter monsoon and Arctic Oscillation: A comparison of 1950–1970 and 1983–2012. *J Clim* 27:5075–5091. <https://doi.org/10.1175/JCLI-D-13-00335.1>
- Li F, Wang HJ, Gao YQ (2015) Change in sea ice cover is responsible for non-uniform variation in winter temperature over East Asia. *Atmos Oceanic Sci Lett* 8:376–382. <https://doi.org/10.3878/AOSL20150039>
- Lin ZD, Li F (2018) Impact of interannual variations of spring sea ice in the Barents Sea on East Asian rainfall in June. *Atmos Oceanic Sci Lett* 11:275–281. <https://doi.org/10.1080/16742834.2018.1454249>
- Liu JP, Curry JA, Wang HJ, Song MR, Horton RM (2012) Impact of declining Arctic sea ice on winter snowfall. *Proc Natl Acad Sci U S A* 109:4074–4079. <https://doi.org/10.1073/pnas.1114910109>
- Liu Y, Coauthors, (2020) Role of Autumn Arctic Sea Ice in the subsequent Summer Precipitation variability over East Asia. *Int J Climatol* 40:706–722. <https://doi.org/10.1002/joc.6232>
- Liu Y, Chen HP, Wang HJ, Sun JQ, Li H, Qiu YB (2019) Modulation of the Kara Sea ice variation on the ice freeze-up time in Lake Qinghai. *J Clim* 32:2553–2568. <https://doi.org/10.1175/JCLI-D-18-0636.1>
- Lu RY, Oh JH, Kim BJ (2002) A teleconnection pattern in upper-level meridional wind over the North African and Eurasian continent in summer. *Tellus* 54A:44–55. <https://doi.org/10.1034/j.1600-0870.2002.00248x>
- Parkinson CL, Cavalieri DJ, Gloersen P, Zwally HJ, Comiso JC (1999) Arctic sea ice extents, areas, and trends, 1978–1996. *J Geophys Res: Ocean* 104:20837–20856. <https://doi.org/10.1029/1999JC900082>
- Petoukhov V, Semenov VA (2010) A link between reduced Barents-Kara sea ice and cold winter extremes over northern continents. *J Geophys Res: Atmos* 115:D21111. <https://doi.org/10.1029/2009JD013568>
- Plumb RA (1985) On the three-dimensional propagation of stationary waves. *J Atmos Sci* 42:217–229. [https://doi.org/10.1175/1520-0469\(1985\)042<3c0217:OTTDPO%3e2.0.CO;2](https://doi.org/10.1175/1520-0469(1985)042<3c0217:OTTDPO%3e2.0.CO;2)
- Rayner NA, Coauthors, (2003) Global analyses of sea surface temperature, sea ice, and night marine air temperature since the late nineteenth century. *J Geophys Res* 108:4407. <https://doi.org/10.1029/2002JD002670>
- Sardeshmukh PD, Hoskins BJ (1988) The generation of global rotational flow by steady idealized tropical divergence. *J Atmos Sci* 45:1228–1251. [https://doi.org/10.1175/1520-0469\(1988\)045<3c1228:TGOGRF%3e2.0.CO;2](https://doi.org/10.1175/1520-0469(1988)045<3c1228:TGOGRF%3e2.0.CO;2)
- Serreze MC, Holland MM, Stroeve J (2007) Perspectives on the Arctic's shrinking sea ice cover. *Science* 315:533–536. <https://doi.org/10.1126/science.1139426>
- Serreze MC, Meier WN (2019) The Arctic's sea ice cover: trends, variability, predictability, and comparisons to the Antarctic. *Annals New York Academy Sci* 1436:36–53. <https://doi.org/10.1111/nyas.13856>
- Shen BZ, Lin ZD, Lu RY, Lian Y (2011) Circulation anomalies associated with interannual variation of early- and late-summer precipitation in Northeast China. *Sci China Earth Sci* 54:1095–1104. <https://doi.org/10.1007/s11430-011-4173-6>
- Sun JQ, Wang HJ (2012) Changes of the connection between the summer North Atlantic Oscillation and the East Asian summer rainfall. *J Geophys Res* 117:D08110. <https://doi.org/10.1029/2012JD017482>
- Sun L, Shen BZ, Sui B, Huang BH (2017) The influences of East Asian summer monsoon on summer precipitation in Northeast China. *Clim Dyn* 48:1657–1659. <https://doi.org/10.1007/s00382-016-3165-9>
- Tetzlaff A, Kaleschke L, Lüpkes C, Ament F, Vihma T (2013) The impact of heterogeneous surface temperatures on the 2-m air temperature over the Arctic Ocean under clear skies in spring. *Cryosphere* 7:153–166. <https://doi.org/10.5194/tc-7-153-2013>
- Wei JF, Zhang XD, Wang ZM (2019) Reexamination of Fram Strait sea ice export and its role in recently accelerated Arctic sea ice retreat. *Clim Dyn* 53:1823–1841. <https://doi.org/10.1007/s00382-019-04741-0>

- Wang HJ, Chen HP, Liu JP (2015) Arctic sea ice decline intensified haze pollution in eastern China. *Atmos Oceanic Sci Lett* 8:1–9. <https://doi.org/10.3878/AOSL20140081>
- Wang HJ, He SP (2015) The North China/Northeastern Asia severe summer drought in 2014. *J Clim* 28:6667–6681. <https://doi.org/10.1175/JCLI-D-15-0202.1>
- Wang ZY, Ding YH (2009) Impacts of the long-term change of the summer Asian polar vortex on the circulation system and the water vapor transport in East Asia. *Chin J Geophys* 52:20–29
- Wu BY, Zhang RH, D'Arrigo R (2008) Arctic dipole anomaly and summer rainfall in Northeast China. *Chin Sci Bull* 53:2222–2229
- Wu BY, Zhang RH, Wang B, D'Arrigo R (2009) On the association between spring Arctic sea ice concentration and Chinese summer rainfall. *Geophys Res Lett* 36:L09501. <https://doi.org/10.1029/2009GL037299>
- Wu J, Gao XJ (2013) A gridded daily observation dataset over China region and comparison with the other datasets. *Chin J Geophys* 56:1102–1111
- Xu ZQ, Fan K, Wang HJ (2015) Decadal variation of summer precipitation over China and associated atmospheric circulation after the Late 1990s. *J Clim* 28:4086–4106. <https://doi.org/10.1175/JCLI-D-14-00464.1>
- Yao XP, Dong M (2000) Research on the features of summer rainfall in Northeast China. *Quarterly J Appl Meteor* 11:297–303. <https://doi.org/10.3969/j.issn.1001-7313.2000.03.006>
- Yasui S, Watanabe M (2010) Forcing processes of the summertime circumglobal teleconnection pattern in a dry AGCM. *J Clim* 23:2093–2114. <https://doi.org/10.1175/2009JCLI3323.1>
- Zhang PF, Coauthors, (2018) A stratospheric pathway linking a colder Siberia to Barents-Kara Sea sea ice loss. *Sci Adv*. 4:eaat6025. <https://doi.org/10.1126/sciadv.aat6025>
- Zhou BT, Xu Y, Wu J, Dong SY, Shi Y (2016) Changes in temperature and precipitation extreme indices over China: Analysis of a high-resolution grid dataset. *Int J Climatol* 36:1051–1066. <https://doi.org/10.1002/joc.4400>

Publisher's Note Springer Nature remains neutral with regard to jurisdictional claims in published maps and institutional affiliations.